

Aggregation State of Metal-Based Nanomaterials at the Pulmonary Surfactant Film Determines Biophysical Inhibition

Yi Yang,^{†,‡} Lu Xu,^{†,‡} Susan Dekkers,^{‡,§} Lijie Grace Zhang,^{||} Flemming R. Cassee,^{*,‡,§} and Yi Y. Zuo^{*,†,⊥}

[†]Department of Mechanical Engineering, University of Hawaii at Manoa, Honolulu, Hawaii 96822, United States

[‡]National Institute for Public Health and the Environment, 3720 BA, Bilthoven, The Netherlands

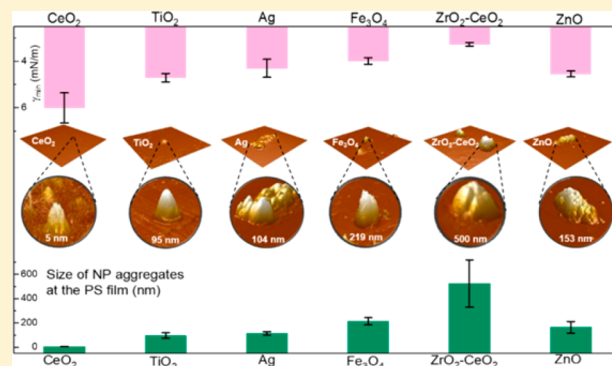
[§]Institute of Risk Assessment Sciences, Utrecht University, 3508 TD, Utrecht, The Netherlands

^{||}Departments of Mechanical and Aerospace Engineering, Biomedical Engineering, and Medicine, The George Washington University, Washington, D.C. 20052, United States

[⊥]Department of Pediatrics, John A. Burns School of Medicine, University of Hawaii, Honolulu, Hawaii 96826, United States

Supporting Information

ABSTRACT: Metal-based nanomaterials (MNMs) represent a large category of the engineered nanomaterials, and have been extensively used to enhance the electrical, optical, and magnetic properties of nanoenabled consumer products. Inhaled MNMs can penetrate deeply into the peripheral lung at which they first interact with the pulmonary surfactant (PS) lining of alveoli. Here we studied the biophysical inhibitory potential of representative MNMs on a modified natural PS, Infasurf, using a novel in vitro experimental methodology called the constrained drop surfactometry (CDS). It was found that the biophysical inhibitory potential of six MNMs on Infasurf ranks in the order $\text{CeO}_2 > \text{ZnO} > \text{TiO}_2 > \text{Ag} > \text{Fe}_3\text{O}_4 > \text{ZrO}_2\text{-CeO}_2$. This rank of in vitro biophysical inhibition is in general agreement with the in vitro and in vivo toxicity of these MNMs. Directly imaging the lateral structure and molecular conformation of the PS film using atomic force microscopy revealed that there exists a correlation between biophysical inhibition of the PS film by the MNMs and their aggregation state at the PS film. Taken together, our study suggests that the nano–bio interactions at the PS film are determined by multiple physicochemical properties of the MNMs, including not only well-studied properties such as their chemical composition and particle size, but also properties such as hydrophobicity, dissolution rate, and aggregation state at the PS film found here. Our study provides novel insight into the understanding of nanotoxicology and metallomics of MNMs.



INTRODUCTION

With the increasing application of engineered nanomaterials (ENMs) in various industrial areas and consumer products, such as electronics, cosmetic, coating and spray, food and medicine, the study of potential environmental, health, and safety (EHS) impacts of the ENMs has grown into an active research field.^{1–4} The small size of ENMs and other unique properties and behavior, such as their large surface area-to-volume ratio,⁵ enable them to penetrate a range of biological barriers of the human body, including the skin, the ocular surface,⁶ the alveolar–capillary barrier,⁷ the blood–brain barrier,⁸ and even the blood–placental barrier.⁹ Although researchers are taking advantage of these nano–bio interactions for designing enhanced drug delivery vehicles,^{10,11} many nano–bio interactions have demonstrated detrimental biological impacts such as generation of reactive oxidative species (ROS), cytotoxicity, genotoxicity, and inflammatory responses, depending on the dose of exposure.^{1–4}

In particular, plenty of evidence shows that inhaled ENMs penetrate deeply into the peripheral lung at which they first interact with the pulmonary surfactant (PS) lining of the alveoli.^{12,13} The PS is composed of approximately 90 wt % lipids, including 90–95% phospholipids and 5–10% cholesterol, and 10 wt % surfactant-associated proteins.¹⁴ It forms a thin film at the air–water interface of alveoli by adsorption. The major physiological and biophysical function of the PS film is to reduce the alveolar surface tension to near-zero value, thus maintaining a large surface area of the alveolar–capillary membrane to facilitate respiration.¹⁴ Numerous in vivo, in vitro, and in silico studies have shown that various ENMs, including nanoenabled consumer products, inhibit the biophysical function of the PS, i.e., abolish its ability in

Received: June 1, 2018

Revised: July 11, 2018

Accepted: July 16, 2018

Published: July 16, 2018

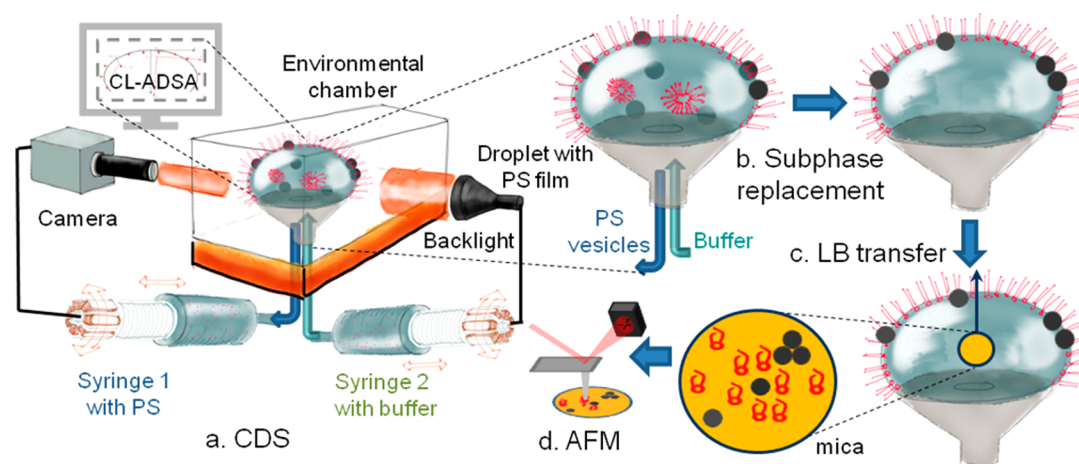


Figure 1. Schematic of the constrained drop surfactometry (CDS) for studying nano–bio interactions at the surface of pulmonary surfactant (PS) films. (a) CDS uses the air–water interface of a 3–4 mm sessile drop, constrained on a sharp pedestal, to accommodate the adsorbed PS film. The PS film can be periodically compressed and expanded by precisely regulating liquid flow into and out of the droplet with a motorized syringe. The surface tension and surface area of the PS film are simultaneously determined from the shape of the droplet using newly developed closed-loop axisymmetric drop shape analysis (CL-ADSA). The droplet is enclosed in an environmental control chamber that permits simulation of physiological conditions. (b) Subphase replacement was implemented with a coaxial pedestal system through which the PS vesicles were slowly withdrawn from the droplet and simultaneously replaced with an equal amount of buffer injected into the droplet. As a result, the liquid hypophase beneath the air–water interface was washed without disturbing the adsorbed PS film at the air–water interface. (c) The adsorbed PS film was Langmuir–Blodgett (LB) transferred from the air–water interface onto a freshly peeled mica surface. (d) Topographical images of the immobilized PS films were obtained by atomic force microscopy (AFM).

reducing surface tension.^{12,15–22} As a result of increasing alveolar surface tension, intratrachally administrated ENMs caused significant pulmonary toxicity, revealed by massive lung collapse and infiltration of inflammatory cells into the alveolar space.^{23,24}

Metal-based nanomaterials (MNMs) represent a large category of the ENMs, and have been extensively used to enhance the electrical, optical, and magnetic properties of nanoenabled consumer products.²⁵ The EHS impacts of MNMs are well studied, under both the scopes of nanotoxicology^{25,26} and metallomics.^{27,28} In spite of the extensive study of MNMs, their potential biophysical influence on the natural PS is still largely unknown. It is unclear how MNMs interact with the PS film, and how this nano–bio interaction affects both the inhaled MNMs and the innate PS lining layer of the lung.

Here, we studied the *in vitro* biophysical interaction between an animal-derived modified natural PS (i.e., Infasurf) and several representative MNMs, using an experimental methodology called the constrained drop surfactometry (CDS) recently developed in our laboratory.^{21,24} The CDS is a new generation of droplet-based tensiometry technique that allows high-fidelity biophysical simulation of the PS under physiologically relevant conditions.^{21,24} It has been used for studying nano–bio interactions at the surface of PS films.^{20–24} In this study, we focused on five representative MNMs, i.e., silver (Ag), zinc oxide (ZnO), titanium dioxide (TiO₂), iron (II,III) oxide (Fe₃O₄), and cerium dioxide (CeO₂) nanoparticles (NPs). Nano Ag is one of the most commonly used and well studied MNMs, primarily for its antimicrobial properties.²⁵ Both ZnO and TiO₂ NPs have been widely used in sunscreens.^{25,26} Fe₃O₄ NPs have been extensively used in biomedical applications, including magnetic imaging and drug delivery.^{29,30} CeO₂ is an important rare-earth metal oxide, and has been extensively used for polishing and computer chip manufacturing, as well as a fuel additive.^{25,31} It was found that

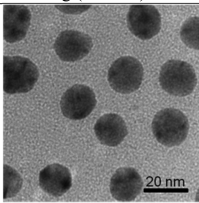
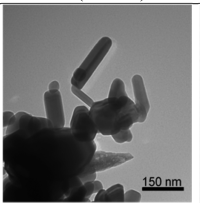
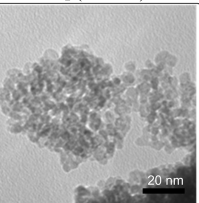
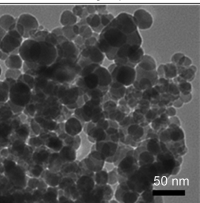
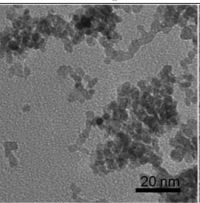
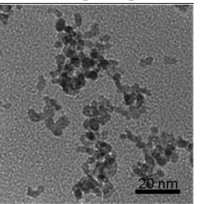
CeO₂ NPs exhibited an adverse effect on bacteria at low environmentally relevant concentrations.³² *In vitro* and *in vivo* toxicity of these MNMs have been well documented.^{25,26,33} In addition to these five benchmark MNMs, we have included in this study CeO₂ NPs doped with 78% zirconium oxide (ZrO₂–CeO₂), enlightened by our recent study showing that Zr-doping significantly reduced the cytotoxicity of CeO₂ NPs *in vitro*, but had only limited effect on pulmonary and cardiovascular systems observed in mice after inhalation.³⁴

■ MATERIALS AND METHODS

Pulmonary Surfactant (PS). Infasurf was a gift from ONY, Inc. (Amherst, NY). It is a modified natural surfactant prepared from lung lavage of newborn calves with centrifugation and organic extraction. Infasurf contains all hydrophobic components of the bovine natural surfactant.³⁵ Hydrophilic surfactant proteins (SP-A and SP-D) were removed during the extraction process. Infasurf was stored at –20 °C in sterilized vials at an initial concentration of 35 mg of total phospholipids per mL. On the day of experiment, it was diluted by a saline buffer (0.9% NaCl, 1.5 mM CaCl₂, and 2.5 mM HEPES, pH 7.0) to a final phospholipid concentration of 1 mg/mL.

Metal-Based Nanomaterials (MNMs). Three benchmark MNMs, i.e., Ag (Series No. NM300), ZnO (NM110), and TiO₂ (NM101) NPs were obtained from the European Commission's Joint Research Centre repository of representative industrial nanomaterials.^{36–38} The Fe₃O₄, CeO₂, and CeO₂ NPs doped with 78% ZrO₂ (ZrO₂–CeO₂) were synthesized with supercritical water hydrothermal synthesis by Promethean Particles (Nottingham, UK) within the EU FP 7 project NanoMILE.^{39,40} Because the antioxidant properties of CeO₂ are primarily due to its ability to scavenge free radicals by switching from the Ce³⁺ to Ce⁴⁺ valence state, incorporation of ZrO₂ into the CeO₂ lattice is expected to reduce the toxicity of CeO₂ by enhancing its antioxidant efficacy.^{34,41} The Ce³⁺/

Table 1. Characterization of Physicochemical Properties of the Metal-Based Nanomaterials (MNMs) Used in This Study^a

Metal-based nanomaterial (MNM)	Nano Silver Ag (NM300)*	Zinc oxide ZnO (NM110)*	Titanium dioxide TiO ₂ (NM101)*	Ferric oxide Fe ₃ O ₄	Cerium dioxide CeO ₂	Cerium dioxide doped 78% zirconium dioxide ZrO ₂ -CeO ₂
Morphology						
Primary size (nm)	17.0 ± 7.6	124.0 ± 55.0	5.0 ± 1.8	29.2 ± 7.7	4.5 ± 1.7	5.0 ± 2.4
Hydrodynamic size (nm)	27 ± 0.1	412 ± 7	843 ± 29 ⁴⁶	1487 ± 165	172 ± 2	358 ± 6
Polydispersity index	0.471 ± 0.004	0.239 ± 0.021	0.30 ± 0.05 ⁴⁶	0.310 ± 0.079	0.272 ± 0.009	0.492 ± 0.029
Hydrophobicity (mL/m ²)	0.026 ± 0.005	-	0.124 ± 0.018	0.016 ± 0.018	0.480 ± 0.065	0.275 ± 0.008
Ce ³⁺ /Ce ⁴⁺	-	-	-	-	0.87	1.40

^a* Indicates series number for the European Commission's Joint Research Centre repository of representative industrial nanomaterials.

Ce⁴⁺ ratio of the CeO₂ with and without ZrO₂ doping was determined with UV/vis spectrophotometry (Jenway 6800, Staffordshire, UK) where Ce³⁺ absorbs in the 230–260 nm range and Ce⁴⁺ absorbs in the 300–400 nm range. All MNMs were characterized with transmission electron microscopy (TEM, Hitachi HT7700) and dynamic light scattering (DLS) (Malvern Zetasizer 5000) to determine the primary and hydrodynamic particle sizes, respectively.

Constrained Drop Surfactometry (CDS). The CDS is a new generation of droplet-based tensiometry technique for biophysical study of PS. Detailed descriptions of the CDS can be found elsewhere.^{21,24} As shown in Figure 1, the CDS uses the air–water interface of a 3–4 mm sessile drop to accommodate the adsorbed PS film. The sessile drop is “constrained” on a carefully machined drop pedestal using a sharp knife-edge to prevent film leakage even at near-zero surface tension. To simulate normal tidal breathing, the adsorbed PS film is periodically compressed and expanded at a physiologically relevant rate and compression ratio by precisely regulating liquid flow into and out of the droplet with a motorized syringe. The surface tension and surface area of the PS film are simultaneously determined from the shape of the droplet using newly developed closed-loop axisymmetric drop shape analysis (CL-ADSA).⁴² Owing to system miniaturization, the droplet is small enough to be enclosed in an environmental control chamber that permits simulation of physiological conditions, i.e., the core body temperature of 37 °C and a relative humidity close to 100%.

Specifically, 1 mg/mL Infasurf was mixed with the MNMs to a final particle concentration of 10 µg/mL, i.e., 1 wt % of total phospholipids in Infasurf. This corresponds to the lower-end particle concentration used in most nanotoxicological studies. The mixtures were incubated at 37 °C for 1 h prior to the biophysical assay. A droplet (~16 µL) of the mixture was dispensed onto a 4-mm CDS pedestal. After droplet formation, the surface tension was recorded and found to quickly decrease to an equilibrium value around 22 mN/m, indicating formation of the adsorbed surfactant film at the air–water interface of the droplet.¹⁴ The adsorbed surfactant film was then compressed and expanded at a rate of 3 s per cycle with a compression ratio

controlled at no more than 25% of the initial surface area to simulate normal tidal breathing.⁴³ To obtain the absolute minimum surface tension of the surfactant film, over-compression at 30%, 35%, and 40% compression ratios were also tested. Biophysical properties of the PS film were quantified with the minimum surface tension (γ_{\min}) at the end of compression, and the average isothermal film compressibility, $\kappa = \frac{1}{A} \left(\frac{\partial A}{\partial \gamma} \right)_T$, during both the compression and expansion processes.¹⁴

Subphase Replacement and in Situ Langmuir–Blodgett (LB) Transfer. To directly visualize the lateral structure and molecular conformation of the adsorbed PS film, we developed a combined technology of subphase replacement and in situ LB transfer from the droplet.^{21,44} As shown in Figure 1, first, the subphase replacement was implemented with a coaxial CDS pedestal through which the PS vesicles were slowly withdrawn from the droplet and simultaneously replaced with an equal amount of buffer injected into the droplet. As a result, the liquid hypophase beneath the air–water interface (i.e., the droplet) was washed without disturbing the adsorbed PS film at the air–water interface, indicated by an unchanged surface tension during the subphase replacement process. Second, after the subphase replacement, LB transfer of the PS film was implemented by lifting a small piece of a freshly peeled mica sheet across the air–water interface of the droplet at a speed of 1 mm/min. The transfer ratio was estimated to be close to unity.

Atomic Force Microscopy (AFM). Topographical images of the immobilized PS films were obtained using an Innova AFM (Bruker, Santa Barbara, CA). Samples were scanned in air with the tapping mode using a silicon cantilever with a resonance frequency of 300 kHz and a spring constant of 42 N/m. The samples were scanned at multiple locations to ensure representativeness and reproducibility. Lateral structures of the samples were analyzed and three-dimensional renderings were produced using Nanoscope Analysis (version 1.5).

Rose Bengal (RB) Partitioning. Relative hydrophobicity of the MNMs was determined using the RB partitioning

method as previously described.^{17,20,45} Briefly, the RB reagent (Sigma-Aldrich, St. Louis, MO) was diluted to 20 $\mu\text{g}/\text{mL}$ using 0.1 M phosphate buffer at pH 7.4. The MNMs at various particle concentrations were added to the solution to create a series of RB-MNM suspensions. Each suspension was incubated at 25 $^{\circ}\text{C}$ for 3 h and subsequently centrifuged at 16 000g for 1 h. The supernatants were collected, and the absorbance at 543 nm was determined with a UV/vis spectrophotometer (Epoch, BioTek, Winooski, VT). Partitioning quotient (PQ) was calculated by the ratio of RB bound onto the particle surface (RB_{bound}) to the free RB in the liquid phase (RB_{free}), i.e., $\text{PQ} = \text{RB}_{\text{bound}}/\text{RB}_{\text{free}}$. Relative hydrophobicity of the MNMs was ranked based on the slope of the linear regression of the plot of PQ vs surface area of the MNMs, where a larger slope indicates a more hydrophobic MNM.

Statistical Analysis. All results are shown as mean \pm standard deviation ($n > 3$). One-way ANOVA with the Tukey means comparison test was used to determine group differences (OriginPro, Northampton, MA). $p < 0.05$ was considered to be statistically significant.

RESULTS

Characterization of the MNMs. Table 1 summarizes characterization results of the six MNMs, i.e., Ag, ZnO, TiO_2 , Fe_3O_4 , CeO_2 , and $\text{ZrO}_2\text{-CeO}_2$. The Ag, TiO_2 , Fe_3O_4 , CeO_2 , and $\text{ZrO}_2\text{-CeO}_2$ NPs have a nearly spherical shape with the primary sizes of 17, 5, 29, 4.5, and 5 nm, respectively. The ZnO NPs have a rod shape with the length of 124 nm. Please refer to Figure S1 of the Supporting Information (SI) for additional TEM micrographs. The average hydrodynamic diameters of these MNMs in buffer are 27, 412, 843, 1487, 172, and 358 nm, respectively, indicating aggregations for all six MNMs. The polydispersity indexes of these NPs are in general less than 0.5, indicating a moderate monodispersity.^{46,47} The significantly larger aggregations of the Fe_3O_4 NPs than the other NPs are most likely due to their magnetic nature.²⁹ As shown in Figure 2, the relative hydrophobicity of these NPs ranks $\text{CeO}_2 > \text{ZrO}_2\text{-CeO}_2 > \text{TiO}_2 > \text{Ag} \approx \text{Fe}_3\text{O}_4$. The ZnO NPs failed the RB partitioning method due to extremely rapid particle aggregation and precipitation in the RB solution. Table 1 also shows the $\text{Ce}^{3+}/\text{Ce}^{4+}$ ratio of the two CeO_2 based MNMs. It is clear that doping CeO_2 with 78% ZrO_2 significantly increases the $\text{Ce}^{3+}/\text{Ce}^{4+}$ ratio from 0.87 to 1.40, indicating an increased antioxidant potential with the ZrO_2 doping.

Biophysical Simulations of Surfactant Inhibition. We first studied the biophysical inhibition of a natural PS, Infasurf, by the MNMs. Figure 3 shows the comparison of the typical compression–expansion cycles of Infasurf with and without MNMs. Reproducibility of these results can be found in SI Figure S2. To simulate normal tidal breathing,⁴³ the surface area of the PS film was oscillated within 25% of the initial surface area, i.e., at a 25% compression ratio (CR), during these dynamic cycling experiments. Compared with pure Infasurf, all MNMs, at a very low particle concentration of 10 $\mu\text{g}/\text{mL}$, increase the minimum surface tension at the end of compression, thus indicating surfactant inhibition.

The statistical analysis of the isothermal film compressibility (κ) during the compression and expansion processes of the dynamic cycling is shown in Figure 4. Film compressibility measures the “hardness” of a two-dimensional film. A low κ indicates a “hard” film, while a high κ indicates a “soft” film. A good pulmonary surfactant film should have a “soft-yet-strong”

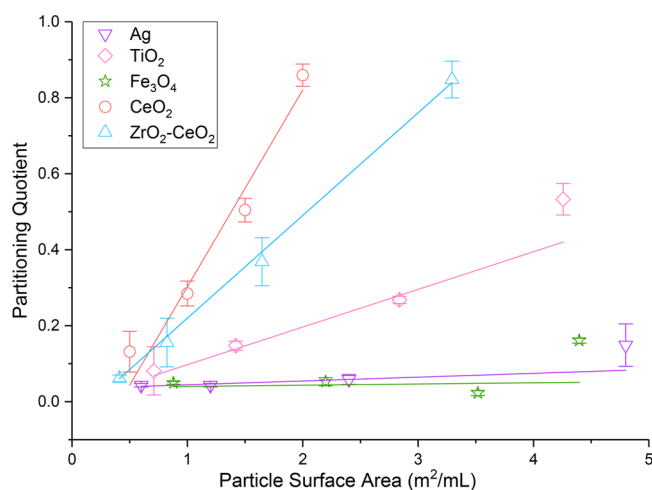


Figure 2. Relative surface hydrophobicity of the five metal-based nanomaterials (MNMs), i.e., Ag, TiO_2 , Fe_3O_4 , CeO_2 , and $\text{ZrO}_2\text{-CeO}_2$, determined with the Rose Bengal partitioning method. Linear regression of the partitioning quotient vs surface area of the MNMs are plotted where the slope is proportional to the relative hydrophobicity of the MNMs. The measurements suggest that the relative surface hydrophobicity of these five MNMs ranks as $\text{CeO}_2 > \text{ZrO}_2\text{-CeO}_2 > \text{TiO}_2 > \text{Ag} \approx \text{Fe}_3\text{O}_4$. The results from ZnO are not included in this figure because ZnO NPs failed the RB partitioning method due to extremely rapid particle aggregation and precipitation in the RB solution.

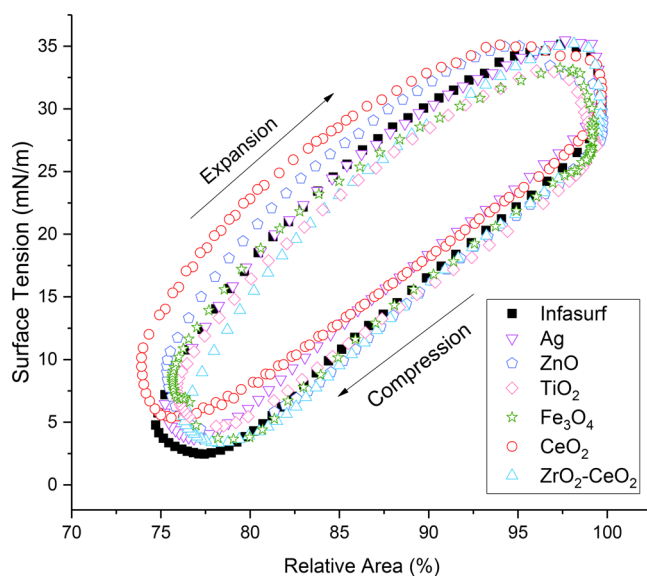


Figure 3. Comparison of the dynamic cycling results of 1 mg/mL Infasurf with and without 1 wt % MNMs. These dynamic compression–expansion cycling experiments closely mimic exhalation and inhalation during normal tidal breathing, i.e., 20 times per minute and maximum 25% surface area variation during cycling. Experimental results were obtained with the CDS under physiologically relevant conditions, i.e., 37 $^{\circ}\text{C}$ and 100% relative humidity. Results shown are the tenth compression–expansion cycle. Biophysical inhibition of Infasurf by the addition of MNMs is evident as shown by increasing minimum surface tension at the end of compression.

attribute.^{14,20} Upon film compression during exhalation, the surfactant film should have a low κ , thus decreasing the alveolar surface tension to low values with only limited area reduction; while upon film expansion during inhalation, the surfactant film should have a high κ , thus only increasing the surface

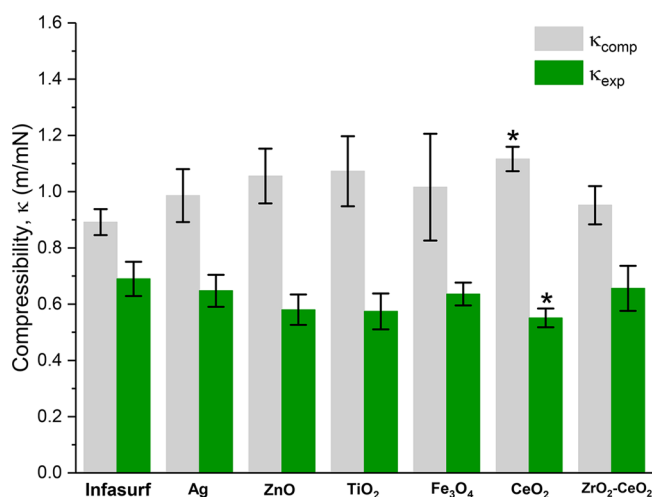


Figure 4. Statistical analysis of the film compressibility during the compression (κ_{comp}) and expansion (κ_{exp}) processes. Experimental results were obtained with the CDS under physiologically relevant conditions. Results shown are the tenth compression–expansion cycle. Biophysical inhibition of Infasurf by the addition of MNMs is evident as shown by increasing κ_{comp} and decreasing κ_{exp} . Among all MNMs, CeO₂ NPs show the highest degree of surfactant inhibition ($p < 0.05$ in comparison with the pure Infasurf).

tension to a limited value with increasing surface area.^{14,20} Therefore, κ is commonly used to evaluate the extent of surfactant inhibition.^{14,20,48} As shown in Figure 4, all MNMs increase the κ of the Infasurf film upon compression (κ_{comp}) and decrease the κ upon expansion (κ_{exp}), with CeO₂ NPs causing the highest degree of surfactant inhibition.

Figure 5 shows the statistical analysis of the minimum surface tension (γ_{min}) of Infasurf, obtained at the tenth cycle,

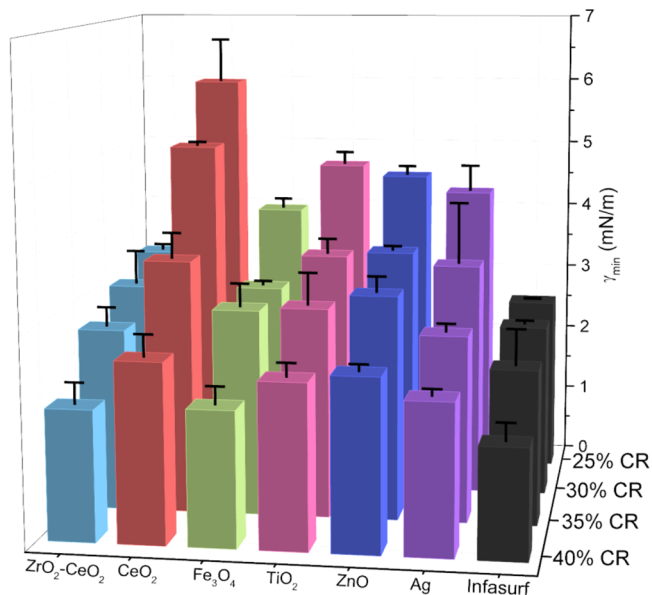


Figure 5. Minimum surface tension (γ_{min}) as a function of the compression ratio (CR). It can be seen that at the physiologically relevant 25% CR, the addition of 1 wt % MNMs all increases the γ_{min} of pure Infasurf. Increasing the CR from 25% to 40% further decreases the γ_{min} of pure Infasurf. Although the γ_{min} of Infasurf mixed with MNMs also decreases accordingly with increasing CR, the addition of MNMs always increases the γ_{min} in comparison with the pure Infasurf.

with and without addition of the MNMs. In addition to the physiologically relevant 25% CR, we have also conducted dynamic cycling experiments at suprphysiological levels of film compression, i.e., at 30, 35, and 40% CRs. Please refer to SI Figures S3–S5 for reproducibility of these results. It can be seen that at the physiologically relevant 25% CR, the addition of 1 wt % MNMs all increases the γ_{min} of pure Infasurf. Increasing the CR from 25% to 40% further decreases the γ_{min} of pure Infasurf from 2.5 to 1.6 mN/m. The γ_{min} of Infasurf mixed with MNMs also decreases accordingly with increasing CR, but always shows a slightly higher γ_{min} than that of the pure Infasurf.

The variation of the γ_{min} of Infasurf with and without MNMs as a function of the increasing number of consecutive compression–expansion cycles is shown in Figure 6. It can

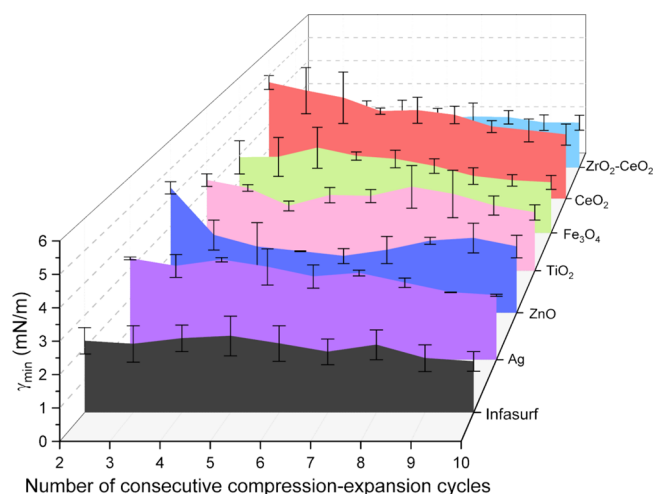


Figure 6. Variation of the minimum surface tension (γ_{min}) with increasing number of consecutive compression–expansion cycles. It can be seen that the pure Infasurf maintains a low γ_{min} in all cycles. However, the addition of MNMs all increases the γ_{min} upon the second cycle. Notably, the γ_{min} of CeO₂ gradually decreases as the number of cycles increases, thus indicating a cycle-dependent removal of the MNMs from the Infasurf film.

be seen that the pure Infasurf reaches a very low γ_{min} of less than 3 mN/m in the second cycle. (Note that results for the first cycle of in vitro tensiometry were usually discarded as they were inconsistent with those of the remaining cycles.⁴⁸) This low γ_{min} is maintained in the subsequent cycles and reaches 1.6 mN/m in the tenth cycle. With the addition of MNMs, especially the CeO₂ NPs, there is a clear trend of gradual surface tension reduction upon increasing number of compression–expansion cycles. It can be seen that the addition of CeO₂ NPs increases the γ_{min} of Infasurf to about 5 mN/m in the second cycle. However, the γ_{min} gradually decreases with increasing number of cycles, and reaches approximately 2 mN/m in the tenth cycle. These surface tension measurements strongly indicate that the MNMs may be squeezed out of the surfactant film with the compression–expansion cycles. We have tested this hypothesis by directly imaging the lateral structure and molecular conformation of the PS film, shown in Figure 7.

Direct Visualization of Nano–Bio Interactions. Topographic images of the Infasurf film with and without exposure to MNMs are shown in Figure 7. The top two rows (Figure 7a–g) show the corresponding 2D and 3D topographic images

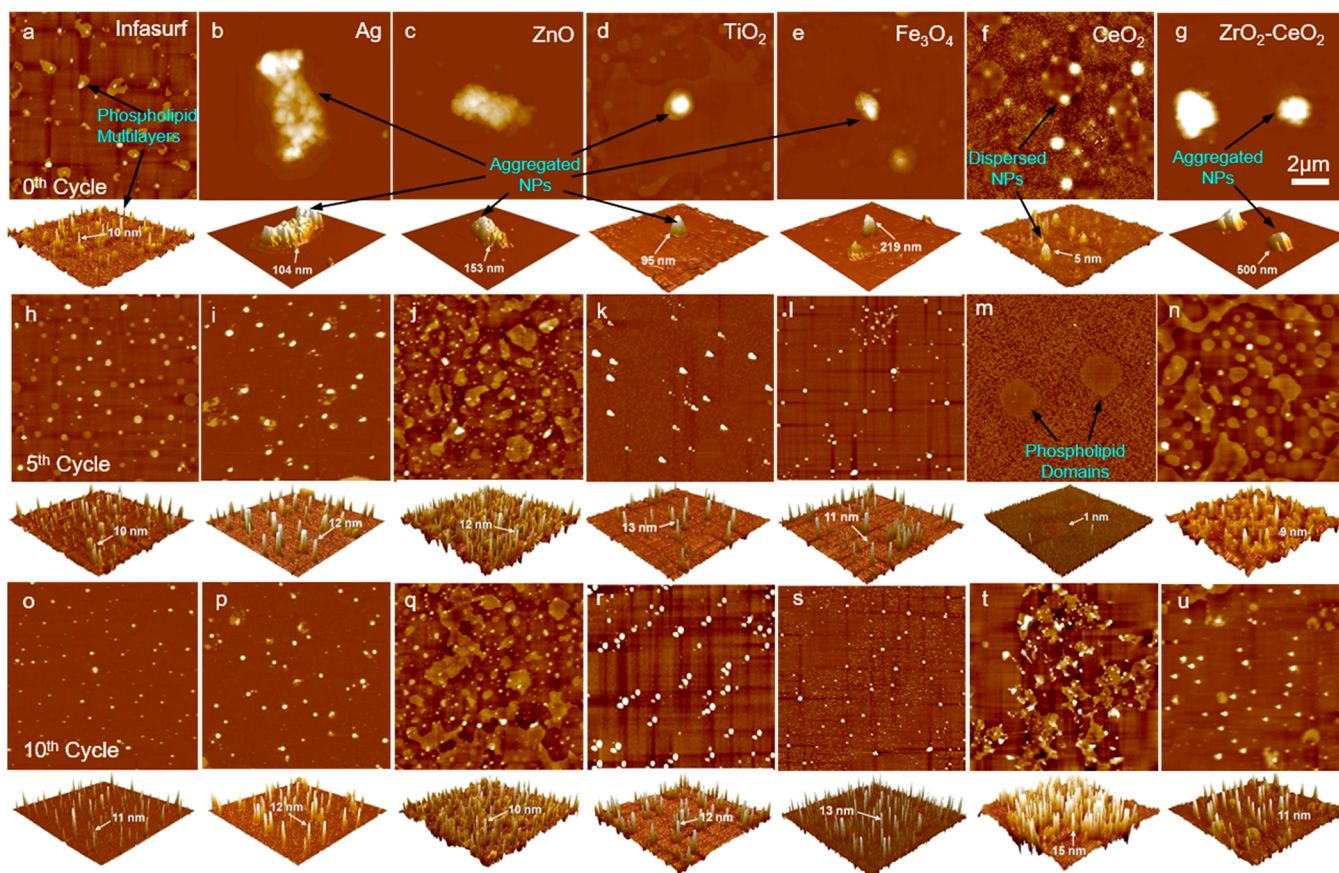


Figure 7. Corresponding 2D and 3D AFM topographic images of the Infasurf film, with and without 1 wt % MNMs, right after de novo adsorption (a–g), after five consecutive compression–expansion cycles (h–n), and after ten consecutive compression–expansion cycles (o–u). All AFM images have the same scanning size of $10 \times 10 \mu\text{m}$. Images in the 1st row have varying z ranges (adapted by the different NP aggregation states at the pulmonary surfactant film) but all images in the 2nd and 3rd rows have the same z range of 20 nm. White arrows denote the height measurements in the AFM images. Black arrows denote specific features detected by the AFM, including the multilayered phospholipid protrusions (~ 10 nm high), phospholipid domains at the monolayer (~ 1 nm higher than the surroundings), individual NPs, and the aggregated NPs.

of the surfactant film right after de novo adsorption (i.e., at the zeroth cycle). Please refer to *SI Figure S6* for additional AFM topographic images that demonstrate the lateral structure of the PS films in a larger scanning area of $50 \times 50 \mu\text{m}$. It can be seen that the adsorbed Infasurf film (Figure 7a) demonstrates a lateral structure of uniformly distributed phospholipid multilayers (~ 10 nm higher than the surroundings). After exposure to MNMs, aggregates of Ag, ZnO, TiO₂, Fe₃O₄, and ZrO₂–CeO₂ NPs (Figure 7b–e, and g) were detected at the de novo adsorbed surfactant films. Different from these MNMs, however, CeO₂ (Figure 7f) mainly appeared as individually dispersed NPs (~ 5 nm high, comparable with their primary particle size shown in Table 1) at the PS film. More importantly, exposure to CeO₂ NPs turned the multilayered PS structure into a monolayer, featuring the formation of phospholipid domains (~ 1 nm higher than the surroundings). The individual CeO₂ NPs were found to be selectively concentrated at the domain boundaries or within the fluid-like liquid-expanded (LE) phase.

The two rows in the middle of Figure 7 (h–n) show the corresponding 2D and 3D topographic images of the surfactant film right after five consecutive compression–expansion cycles (i.e., at the fifth cycle). It is found that the pure Infasurf film maintains the uniform multilayered lateral structure, similar to the lateral structure right after de novo adsorption. Nanoparticles or aggregates of all MNMs are found to be removed

from the Infasurf film by the compression–expansion cycles. The Infasurf film exposed to CeO₂ NPs retains its monolayer conformation (Figure 7m), but the Infasurf films exposed to the other MNMs (Figure 7i–l and n) are able to restore the multilayered structure of the pure Infasurf film.

After another five consecutive compression–expansion cycles (i.e., at the 10th cycle), as shown in the bottom two rows (Figure 7o–u), it is found that all MNMs are removed from the interface and all Infasurf films somehow restore the multilayered lateral structure.

DISCUSSION

Our *in vitro* biophysical simulations (Figures 3–6) consistently suggest that the biophysical inhibitory potential of the six MNMs on the natural PS ranks in the order CeO₂ > ZnO > TiO₂ > Ag > Fe₃O₄ > ZrO₂–CeO₂. This *in vitro* biophysical ranking appears to be in good agreement with *in vitro* and *in vivo* toxicity of these MNMs.^{25,26,34,49–51} Among these NPs, it is well-known that the Fe₃O₄ NPs are largely nontoxic.²⁹ In general, Zn-based NPs were found to have a greater *in vitro* toxicity than many other MNMs.²⁵ In comparative studies Zn-based NPs were not included, Ag NPs were found to have a high cytotoxicity.²⁵ For instance, Kermanizadeh et al. compared the *in vitro* cytotoxicity of the two benchmark MNMs, i.e., Ag (NM300) and ZnO (NM110), in human renal proximal tubule epithelial HK-2 cells since NPs were found to

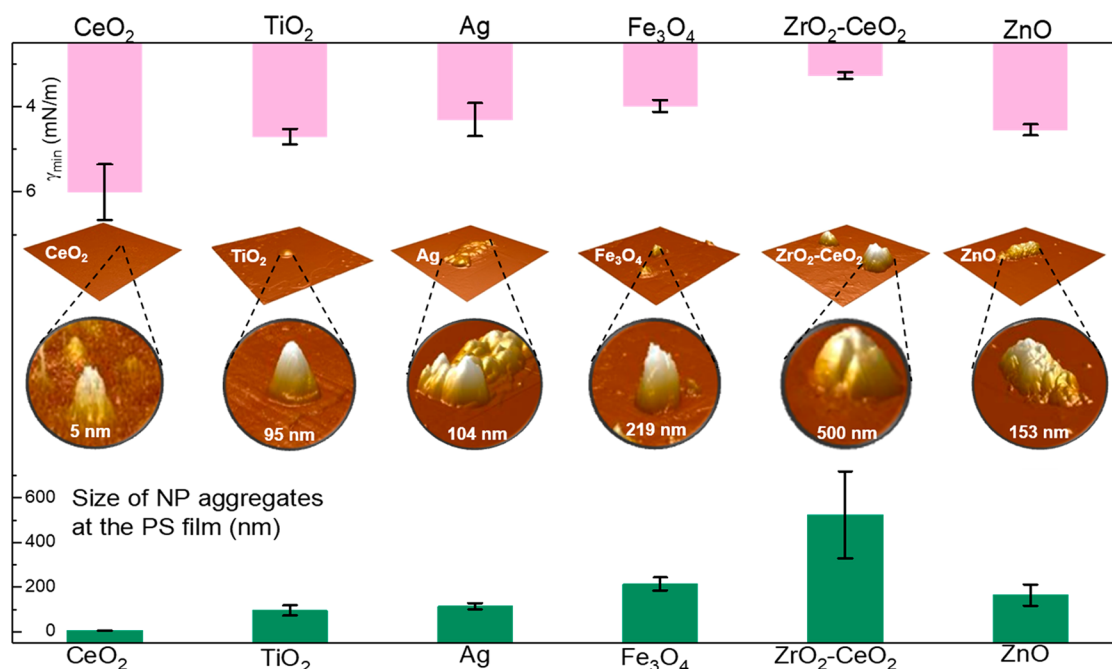


Figure 8. Correlations between pulmonary surfactant (PS) biophysical inhibition and the aggregation state of MNMs at the PS film. Biophysical inhibition of the PS film is measured with the minimum surface tension (γ_{\min}) obtained at the physiologically relevant compression ratio (i.e., 25%). The aggregation state of the MNMs at the PS film was measured with the height profile obtained using AFM right after de novo adsorption. All AFM images have the same scanning size of $10 \times 10 \mu\text{m}$ and a unified z range of 800 nm. The zoomed-in insets show the detailed topographic structure of the aggregated NPs at the PS film.

be primarily accumulated in kidney.⁴⁹ The lethal concentrations killing 50% of the cells with a single exposure (LC_{50}) of Ag and ZnO NPs were determined to be 10 and $2.5 \mu\text{g}/\text{cm}^2$, respectively, after 24 h of exposure. These results indicate that ZnO NPs have a higher toxicity than Ag NPs. Similar findings were reported by Gosens et al. using an acute lung injury model in mice exposed to the same MNMs.⁵⁰ The TiO₂ NPs (NM101) tested in this study have a crystal structure of the anatase phase, which is known to be more toxic than rutile TiO₂ NPs.²⁵ Xia et al. found that the toxicity of anatase TiO₂ NPs is comparable to that of CeO₂ NPs.⁵¹ ZrO₂ in general is nontoxic in the lung.²⁶ Dekkers et al. studied the cytotoxicity of CeO₂ with and without ZrO₂-doping, against human lung epithelial carcinoma A549 cells.³⁴ The EC_{20} , i.e., the effective concentration resulting in 20% cell death, of CeO₂ without and with 78% ZrO₂-doping, was determined to be 0.2 and $33 \mu\text{g}/\text{cm}^2$, respectively, thus indicating that ZrO₂-doping significantly reduces the toxicity of CeO₂. The beneficial effect of ZrO₂-doping was attributed to its antioxidant efficacy as indicated by increasing the $\text{Ce}^{3+}/\text{Ce}^{4+}$ ratio of the CeO₂.^{34,41} Similar effects were found in the present study.

In addition to size and shape of the NPs, the toxicity of MNMs is largely determined by their aggregation state and dissolution rate.^{25–28} Available evidence suggests that natural PS can modify the aggregation state and dissolution kinetics of many MNMs, including CeO₂,⁵² Ag,⁵³ and ZnO,⁵⁴ thus significantly affecting their cytotoxicity, retention, and translocation from the lung. It should be noted that all previous studies on the aggregation state of MNMs were performed in the bulk aqueous phase of natural or model PS.^{53,54} In contrast, for the first time here we directly visualized the aggregation state of MNMs at the surface of the PS film, with combined technological advances in CDS and AFM. It is found that although all MNMs agglomerated significantly in buffer (Table

1), the CeO₂ NPs became well dispersed at the surface of the PS film, while the other MNMs remained agglomerated after interacting with the natural PS (Figure 7). Most interestingly, we found that except for the ZnO NPs, the biophysical inhibitory potential of the MNMs is correlated with the aggregation state of the NPs at the PS film. Here we leave ZnO out of this comparison because it is known that the high toxicity of ZnO NPs is largely due to rapid dissolution in releasing ions.^{51,54}

As summarized in Figure 8, the aggregation size of five MNMs at the PS film, determined with AFM, ranks as $\text{CeO}_2 < \text{TiO}_2 < \text{Ag} < \text{Fe}_3\text{O}_4 < \text{ZrO}_2\text{-CeO}_2$. (Reproducibility of the AFM analysis can be found in SI Figure S7.) Accordingly, the degree of PS inhibition, measured with the minimum surface tension, ranks as $\text{CeO}_2 > \text{TiO}_2 > \text{Ag} > \text{Fe}_3\text{O}_4 > \text{ZrO}_2\text{-CeO}_2$. Therefore, our results suggest that the biophysical inhibition of PS film by NPs, to a great extent, is determined by the aggregation state of the NPs at the PS film. This finding is not unexpected since the dispersed NPs have a much larger surface area, and hence a much higher surface free energy, than aggregated NPs,⁵⁵ thereby possessing a higher potential for adsorbing biomolecules and for causing surfactant inhibition.

Because of their excess surface free energy, upon contact with the natural PS, the surface of NPs is expected to be immediately coated with a PS corona that consists of both phospholipids and surfactant-associated proteins.^{19,56,57} The PS corona determines the biological identity of the inhaled NPs, including their aggregation state and bioactivity. It appears that the PS corona formed on the CeO₂ NPs facilitates dispersion of this MNM to a much larger degree than the other three MNMs, likely due to its high surface hydrophobicity (Figure 2 and Table 1). Our recent molecular dynamics simulations suggested that compared to more hydrophilic NPs, the PS corona formed on hydrophobic NPs is selectively

enriched in the hydrophobic surfactant-associated proteins, SP-B and SP-C.⁵⁶ Once bound to the NP surface, SP-B and/or SP-C is denatured and depleted from the PS film,^{19,58} thereby causing biophysical inhibition of the PS. The depletion of surfactant proteins can be implied from the analysis of PS lateral structures. It is well-known that the multilayered architecture of healthy natural PS films is largely maintained by SP-B and/or SP-C.^{14,35} Therefore, the monolayer structure of the PS film, found at the presence of CeO₂ NPs (Figure 7f and m), strongly indicates deficiency and/or dysfunction of SP-B and/or SP-C. A similar finding was reported by Wang et al., who found that the PS corona facilitated dispersion of single-walled carbon nanotubes (SWCNTs), but did not mitigate their bioactivity and fibrogenic potential.⁵⁹

In summary, we applied a novel in vitro experimental methodology called the constrained drop surfactometry (CDS) in combination with AFM to quantitatively evaluate biophysical inhibition of natural pulmonary surfactant by metal-based nanomaterials (MNMs). Our study showed that interaction with the natural PS film not only affects the biological identity of the MNMs, but also in turn influences the biophysical properties of the PS film. It was found that the biophysical inhibitory potential of the tested MNMs on Infasurf ranks in the order CeO₂ > ZnO > TiO₂ > Ag > Fe₃O₄ > ZrO₂-CeO₂. This rank of in vitro biophysical inhibition is in general agreement with the in vitro and in vivo toxicity of these MNMs. Directly imaging the lateral structure and molecular conformation of the PS film revealed that compared to the other MNMs, the CeO₂ NPs dispersed much better at the PS film, thus preventing the formation of a multilayered architecture required for healthy PS films. There exists a correlation between biophysical inhibition of the PS film by NPs and the aggregation state of the NPs at the PS film. Taking together, our study suggests that the nano-bio interactions at the natural PS film are determined by multiple physicochemical properties of the NPs, including not only the well-studied properties such as their chemical composition and particle size, but also properties such as hydrophobicity, dissolution rate, and aggregation state at the PS film found here. Our study provides novel insight into the understanding of nanotoxicology and metallomics of MNMs.

■ ASSOCIATED CONTENT

Supporting Information

The Supporting Information is available free of charge on the ACS Publications website at DOI: 10.1021/acs.est.8b02976.

Reproducibility of the in vitro biophysical simulations, additional TEM and AFM micrographs (PDF)

■ AUTHOR INFORMATION

Corresponding Authors

*E-mail: yzuo@hawaii.edu.

*E-mail: flemming.cassee@rivm.nl.

ORCID

Susan Dekkers: 0000-0003-2528-863X

Lijie Grace Zhang: 0000-0003-3009-045X

Yi Y. Zuo: 0000-0002-3992-3238

Author Contributions

#Authors Y.Y. and L.X. contributed equally to the content of this paper.

Notes

The authors declare no competing financial interest.

■ ACKNOWLEDGMENTS

We thank Dr. Walter Klein at ONY Inc. for donation of Infasurf samples. This research was supported by the National Science Foundation Grant CBET-1604119 (Y.Y.Z.), the Leahi Fund to Treat & Prevent Pulmonary Diseases from the Hawaii Community Foundation Grant 16ADVC-78729 (Y.Y.Z.), the European Commission Grant NMP4-LA-2013-310451 NANOMILE, and the Dutch Ministry of Infrastructures and Environment (F.R.C.).

■ REFERENCES

- (1) Oberdörster, G.; Oberdörster, E.; Oberdörster, J. Nanotoxicology: an emerging discipline evolving from studies of ultrafine particles. *Environ. Health Perspect.* **2005**, *113* (7), 823–839.
- (2) Nel, A.; Xia, T.; Mädler, L.; Li, N. Toxic potential of materials at the nanolevel. *Science* **2006**, *311* (5761), 622–627.
- (3) Krug, H. F.; Wick, P. Nanotoxicology: An interdisciplinary challenge. *Angew. Chem., Int. Ed.* **2011**, *50* (6), 1260–1278.
- (4) Stone, V.; Miller, M. R.; Clift, M. J. D.; Elder, A.; Mills, N. L.; Moller, P.; Schins, R. P. F.; Vogel, U.; Kreyling, W. G.; Alstrup Jensen, K.; et al. Nanomaterials versus ambient ultrafine particles: An opportunity to exchange toxicology knowledge. *Environ. Health Perspect.* **2017**, *125* (10), 106002.
- (5) Nel, A. E.; Mädler, L.; Velegol, D.; Xia, T.; Hoek, E. M.; Somasundaran, P.; Klaessig, F.; Castranova, V.; Thompson, M. Understanding biophysicochemical interactions at the nano-bio interface. *Nat. Mater.* **2009**, *8* (7), 543–557.
- (6) Prow, T. W. Toxicity of nanomaterials to the eye. *Wiley Interdiscip. Rev.: Nanomed. Nanobiotechnol.* **2010**, *2* (4), 317–333.
- (7) Hidalgo, A.; Cruz, A.; Perez-Gil, J. Pulmonary surfactant and nanocarriers: Toxicity versus combined nanomedical applications. *Biochim. Biophys. Acta, Biomembr.* **2017**, *1859* (9), 1740–1748.
- (8) Kolter, M.; Ott, M.; Hauer, C.; Reimold, I.; Fricker, G. Nanotoxicity of poly(n-butylcyano-acrylate) nanoparticles at the blood-brain barrier, in human whole blood and in vivo. *J. Controlled Release* **2015**, *197*, 165–179.
- (9) Yamashita, K.; Yoshioka, Y.; Higashisaka, K.; Mimura, K.; Morishita, Y.; Nozaki, M.; Yoshida, T.; Ogura, T.; Nabeshi, H.; Nagano, K.; Abe, Y.; Kamada, H.; Monobe, Y.; Imazawa, T.; Aoshima, H.; Shishido, K.; Kawai, Y.; Mayumi, T.; Tsunoda, S.; Itoh, N.; Yoshikawa, T.; Yanagihara, I.; Saito, S.; Tsutsumi, Y. Silica and titanium dioxide nanoparticles cause pregnancy complications in mice. *Nat. Nanotechnol.* **2011**, *6* (5), 321–8.
- (10) Blanco, E.; Shen, H.; Ferrari, M. Principles of nanoparticle design for overcoming biological barriers to drug delivery. *Nat. Biotechnol.* **2015**, *33*, 941–951.
- (11) Ruge, C. A.; Kirch, J.; Lehr, C.-M. Pulmonary drug delivery: from generating aerosols to overcoming biological barriers—therapeutic possibilities and technological challenges. *Lancet Respir. Med.* **2013**, *1* (5), 402–413.
- (12) Fan, Q.; Wang, Y. E.; Zhao, X.; Loo, J. S.; Zuo, Y. Y. Adverse biophysical effects of hydroxyapatite nanoparticles on natural pulmonary surfactant. *ACS Nano* **2011**, *5* (8), 6410–6416.
- (13) Tsuda, A.; Gehr, P. *Nanoparticles in the Lung: Environmental Exposure and Drug Delivery*; CRC Press: Boca Raton, FL, 2015.
- (14) Zuo, Y. Y.; Veldhuizen, R. A.; Neumann, A. W.; Petersen, N. O.; Possmayer, F. Current perspectives in pulmonary surfactant—inhibition, enhancement and evaluation. *Biochim. Biophys. Acta, Biomembr.* **2008**, *1778* (10), 1947–1977.
- (15) Bakshi, M. S.; Zhao, L.; Smith, R.; Possmayer, F.; Petersen, N. O. Metal nanoparticle pollutants interfere with pulmonary surfactant function in vitro. *Biophys. J.* **2008**, *94* (3), 855–868.
- (16) Schleh, C.; Muhlfield, C.; Pulskamp, K.; Schmiedl, A.; Nassimi, M.; Lauenstein, H. D.; Braun, A.; Krug, N.; Erpenbeck, V. J.;

Hohlfeld, J. M. The effect of titanium dioxide nanoparticles on pulmonary surfactant function and ultrastructure. *Respir. Res.* **2009**, *10*, 90.

(17) Beck-Broichsitter, M.; Ruppert, C.; Schmehl, T.; Guenther, A.; Betz, T.; Bakowsky, U.; Seeger, W.; Kissel, T.; Gessler, T. Biophysical investigation of pulmonary surfactant surface properties upon contact with polymeric nanoparticles in vitro. *Nanomedicine* **2011**, *7* (3), 341–350.

(18) Dwivedi, M. V.; Harishchandra, R. K.; Koshkina, O.; Maskos, M.; Galla, H.-J. Size influences the effect of hydrophobic nanoparticles on lung surfactant model systems. *Biophys. J.* **2014**, *106*, 289–298.

(19) Hu, G.; Jiao, B.; Shi, X.; Valle, R. P.; Fan, Q.; Zuo, Y. Y. Physicochemical properties of nanoparticles regulate translocation across pulmonary surfactant monolayer and formation of lipoprotein corona. *ACS Nano* **2013**, *7* (12), 10525–10533.

(20) Valle, R. P.; Huang, C. L.; Loo, J. S.; Zuo, Y. Y. Increasing hydrophobicity of nanoparticles intensifies lung surfactant film inhibition and particle retention. *ACS Sustainable Chem. Eng.* **2014**, *2* (7), 1574–1580.

(21) Valle, R. P.; Wu, T.; Zuo, Y. Y. Biophysical influence of airborne carbon nanomaterials on natural pulmonary surfactant. *ACS Nano* **2015**, *9* (5), 5413–5421.

(22) Sorli, J. B.; Huang, Y.; Da Silva, E.; Hansen, J. S.; Zuo, Y. Y.; Frederiksen, M.; Norgaard, A. W.; Ebbelohj, N. E.; Larsen, S. T.; Hougaard, K. S. Prediction of acute inhalation toxicity using in vitro lung surfactant inhibition. *ALTEX* **2018**, *35* (1), 26–36.

(23) Chen, Y.; Yang, Y.; Xu, B.; Wang, S.; Li, B.; Ma, J.; Gao, J.; Zuo, Y. Y.; Liu, S. Mesoporous carbon nanomaterials induced pulmonary surfactant inhibition, cytotoxicity, inflammation and lung fibrosis. *J. Environ. Sci.* **2017**, *62*, 100–114.

(24) Yang, Y.; Wu, Y.; Ren, Q.; Zhang, L. G.; Liu, S.; Zuo, Y. Y. Biophysical assessment of pulmonary surfactant predicts the lung toxicity of nanomaterials. *Small Methods* **2018**, *2* (4), 1700367.

(25) Schrand, A. M.; Rahman, M. F.; Hussain, S. M.; Schlager, J. J.; Smith, D. A.; Syed, A. F. Metal-based nanoparticles and their toxicity assessment. *Wiley Interdiscip. Rev.: Nanomed. Nanobiotechnol.* **2010**, *2* (5), 544–568.

(26) Landsiedel, R.; Ma-Hock, L.; Kroll, A.; Hahn, D.; Schnekenburger, J.; Wiench, K.; Wohlleben, W. Testing metal-oxide nanomaterials for human safety. *Adv. Mater.* **2010**, *22* (24), 2601–2627.

(27) Wang, B.; Feng, W.; Zhao, Y.; Chai, Z. Metallomics insights for in vivo studies of metal based nanomaterials. *Metallomics* **2013**, *5* (7), 793–803.

(28) Li, Y.-F.; Gao, Y.; Chai, Z.; Chen, C. Nanometallomics: an emerging field studying the biological effects of metal-related nanomaterials. *Metallomics* **2014**, *6* (2), 220–232.

(29) Gupta, A. K.; Gupta, M. Synthesis and surface engineering of iron oxide nanoparticles for biomedical applications. *Biomaterials* **2005**, *26* (18), 3995–4021.

(30) Laurent, S.; Forge, D.; Port, M.; Robic, C.; Vander Elst, L.; Muller, R. N. Magnetic iron oxide nanoparticles: synthesis, stabilization, vectorization, physicochemical characterizations, and biological applications. *Chem. Rev.* **2008**, *108* (6), 2064–110.

(31) Cassee, F. R.; van Balen, E. C.; Singh, C.; Green, D.; Muijsers, H.; Weinstein, J.; Dreher, K. Exposure, health and ecological effects review of engineered nanoscale cerium and cerium oxide associated with its use as a fuel additive. *Crit. Rev. Toxicol.* **2011**, *41* (3), 213–229.

(32) Zhang, H.; He, X.; Zhang, Z.; Zhang, P.; Li, Y.; Ma, Y.; Kuang, Y.; Zhao, Y.; Chai, Z. Nano-CeO₂ exhibits adverse effects at environmental relevant concentrations. *Environ. Sci. Technol.* **2011**, *45* (8), 3725–3730.

(33) Rastogi, A.; Zivcak, M.; Sytar, O.; Kalaji, H. M.; He, X.; Mbarki, S.; Brestic, M. Impact of metal and metal oxide nanoparticles on Plant: A Critical Review. *Front. Chem.* **2017**, *5*, 78.

(34) Dekkers, S.; Miller, M. R.; Schins, R. P. F.; Romer, I.; Russ, M.; Vandebriel, R. J.; Lynch, I.; Belinga-Desaunay, M. F.; Valsami-Jones, E.; Connell, S. P.; et al. The effect of zirconium doping of cerium

dioxide nanoparticles on pulmonary and cardiovascular toxicity and biodistribution in mice after inhalation. *Nanotoxicology* **2017**, *11* (6), 794–808.

(35) Zhang, H.; Fan, Q.; Wang, Y. E.; Neal, C. R.; Zuo, Y. Y. Comparative study of clinical pulmonary surfactants using atomic force microscopy. *Biochim. Biophys. Acta, Biomembr.* **2011**, *1808* (7), 1832–1842.

(36) Klein, C.; Comero, S.; Stahlmecke, B.; Romazanov, J.; Kuhlbusch, T.; Van Doren, E.; De Temmerman, P.; Mast, J.; Wick, P.; Krug, H. *NM-Series of representative manufactured nanomaterials: NM-300 Silver Characterisation, Stability, Homogeneity*; EUR 24693 EN-2011; JRC, European Commission, 2011 DOI: 10.2788/2307.

(37) Singh, C.; Friedrichs, S.; Levin, M.; Birkedal, R.; Jensen, K.; Pojana, G.; Wohlleben, W.; Schulte, S.; Wiench, K.; Turney, T. Zinc Oxide NM-110, NM-111, NM-112, NM-113: characterisation and test item preparation. In *NM-Series of Representative Manufactured Nanomaterials*; Joint Research Centre of the European Commission: Ispra, Italy 2011.

(38) Singh, C.; Friedrichs, S.; Ceccone, G.; Gibson, P.; Jensen, K.; Levin, M.; Goenaga Infante, H.; Carlander, D.; Rasmussen, K. *Cerium Dioxide, NM-211, NM-212, NM-213. Characterisation and Test Item Preparation*; European Commission, Joint Research Centre, Institute for Health and Consumer Protection: Ispra, Italy, 2014.

(39) Cabanas, A.; Darr, J. A.; Lester, E.; Poliakov, M. A continuous and clean one-step synthesis of nano-particulate Ce1-xZrxO₂ solid solutions in near-critical water. *Chem. Commun.* **2000**, *11*, 901–902.

(40) Liu, J.; Romer, I.; Tang, S. V. Y.; Valsami-Jones, E.; Palmer, R. E. Crystallinity depends on choice of iron salt precursor in the continuous hydrothermal synthesis of Fe-Co oxide nanoparticles. *RSC Adv.* **2017**, *7* (59), 37436–37440.

(41) Tsai, Y.-Y.; Oca-Cossio, J.; Lin, S.-M.; Woan, K.; Yu, P.-C.; Sigmund, W. Reactive oxygen species scavenging properties of ZrO₂-CeO₂ solid solution nanoparticles. *Nanomedicine* **2008**, *3* (5), 637–645.

(42) Yu, K.; Yang, J.; Zuo, Y. Y. Automated droplet manipulation using closed-loop axisymmetric drop shape analysis. *Langmuir* **2016**, *32* (19), 4820–4826.

(43) Bachofen, H.; Schurch, S.; Urbinelli, M.; Weibel, E. Relations among alveolar surface tension, surface area, volume, and recoil pressure. *J. Appl. Physiol.* **1987**, *62* (5), 1878–1887.

(44) Li, C.; Xu, L.; Zuo, Y. Y.; Yang, P. Tuning protein assembly pathways through superfast amyloid-like aggregation. *Biomater. Sci.* **2018**, *6* (4), 836–841.

(45) Müller, R. H.; Rühl, D.; Lück, M.; Paulke, B.-R. Influence of fluorescent labelling of polystyrene particles on phagocytic uptake, surface hydrophobicity, and plasma protein adsorption. *Pharm. Res.* **1997**, *14* (1), 18–24.

(46) Di Cristo, L.; Maguire, C. M.; Mc Quillan, K.; Aleardi, M.; Volkov, Y.; Movia, D.; Prina-Mello, A. Towards the identification of an in vitro tool for assessing the biological behavior of aerosol supplied nanomaterials. *Int. J. Environ. Res. Public Health* **2018**, *15* (4), 563.

(47) Bhattacharjee, S. DLS and zeta potential - What they are and what they are not? *J. Controlled Release* **2016**, *235*, 337–351.

(48) Schürch, S.; Green, F. H.; Bachofen, H. Formation and structure of surface films: captive bubble surfactometry. *Biochim. Biophys. Acta, Mol. Basis Dis.* **1998**, *1408* (2), 180–202.

(49) Keramanizadeh, A.; Vranic, S.; Boland, S.; Moreau, K.; Baeza-Squiban, A.; Gaiser, B. K.; Andrzejczuk, L. A.; Stone, V. An in vitro assessment of panel of engineered nanomaterials using a human renal cell line: cytotoxicity, pro-inflammatory response, oxidative stress and genotoxicity. *BMC Nephrol.* **2013**, *14* (1), 96.

(50) Gosens, I.; Keramanizadeh, A.; Jacobsen, N. R.; Lenz, A. G.; Bokkers, B.; de Jong, W. H.; Krystek, P.; Tran, L.; Stone, V.; Wallin, H.; et al. Comparative hazard identification by a single dose lung exposure of zinc oxide and silver nanomaterials in mice. *PLoS One* **2015**, *10* (5), e0126934.

(51) Xia, T.; Kovochich, M.; Liang, M.; Madler, L.; Gilbert, B.; Shi, H.; Yeh, J. I.; Zink, J. I.; Nel, A. E. Comparison of the mechanism of

toxicity of zinc oxide and cerium oxide nanoparticles based on dissolution and oxidative stress properties. *ACS Nano* **2008**, *2* (10), 2121–34.

(52) He, X.; Zhang, H.; Ma, Y.; Bai, W.; Zhang, Z.; Lu, K.; Ding, Y.; Zhao, Y.; Chai, Z. Lung deposition and extrapulmonary translocation of nano-ceria after intratracheal instillation. *Nanotechnology* **2010**, *21* (28), 285103.

(53) Leo, B. F.; Chen, S.; Kyo, Y.; Herpoldt, K. L.; Terrill, N. J.; Dunlop, I. E.; McPhail, D. S.; Shaffer, M. S.; Schwander, S.; Gow, A.; Zhang, J.; Chung, K. F.; Tetley, T. D.; Porter, A. E.; Ryan, M. P. The stability of silver nanoparticles in a model of pulmonary surfactant. *Environ. Sci. Technol.* **2013**, *47* (19), 11232–11240.

(54) Theodorou, I. G.; Ruenraroengsak, P.; Gow, A.; Schwander, S.; Zhang, J. J.; Chung, K. F.; Tetley, T. D.; Ryan, M. P.; Porter, A. E. Effect of pulmonary surfactant on the dissolution, stability and uptake of zinc oxide nanowires by human respiratory epithelial cells. *Nanotoxicology* **2016**, *10* (9), 1351–1362.

(55) Tsuda, A.; Konduru, N. V. The role of natural processes and surface energy of inhaled engineered nanoparticles on aggregation and corona formation. *NanoImpact* **2016**, *2*, 38–44.

(56) Hu, Q.; Bai, X.; Hu, G.; Zuo, Y. Y. Unveiling the Molecular Structure of Pulmonary Surfactant Corona on Nanoparticles. *ACS Nano* **2017**, *11* (7), 6832–6842.

(57) Konduru, N. V.; Molina, R. M.; Swami, A.; Damiani, F.; Pyrgiotakis, G.; Lin, P.; Andreozzi, P.; Donaghey, T. C.; Demokritou, P.; Krol, S.; et al. Protein corona: implications for nanoparticle interactions with pulmonary cells. *Part. Fibre Toxicol.* **2017**, *14* (1), 42.

(58) Mahmoudi, M.; Lynch, I.; Ejtehadi, M. R.; Monopoli, M. P.; Bombelli, F. B.; Laurent, S. Protein– nanoparticle interactions: opportunities and challenges. *Chem. Rev.* **2011**, *111* (9), 5610–5637.

(59) Wang, L.; Castranova, V.; Mishra, A.; Chen, B.; Mercer, R. R.; Schwegler-Berry, D.; Rojanasakul, Y. Dispersion of single-walled carbon nanotubes by a natural lung surfactant for pulmonary in vitro and in vivo toxicity studies. *Part. Fibre Toxicol.* **2010**, *7*, 31.